Research Article

Phan Tu Quy[#], Thanh Q. Bui[#], Nguyen Minh Thai, Ly Nguyen Hai Du, Nguyen Thanh Triet, Tran Van Chen, Nguyen Vinh Phu, Duong Tuan Quang, Dao-Cuong To, Nguyen Thi Ai Nhung*

Combinatory *in silico* investigation for potential inhibitors from *Curcuma sahuynhensis* Škorničk. & N.S. Lý volatile phytoconstituents against influenza A hemagglutinin, SARS-CoV-2 main protease, and Omicron-variant spike protein

https://doi.org/10.1515/chem-2023-0109 received May 16, 2023; accepted July 31, 2023

Abstract: *Curcuma sahuynhensis* Škorničk. & N.S. Lý has been discovered recently whose antiviral potential is unknown, thus deserved for discovery-phase screening. A combination of experimental characterization, quantum calculation, molecular

These authors contributed equally to this work.

* Corresponding author: Nguyen Thi Ai Nhung, Department of Chemistry, University of Sciences, Hue University, Hue City 530000, Vietnam, e-mail: ntanhung@hueuni.edu.vn

Phan Tu Quy: Department of Natural Sciences & Technology, Tay Nguyen University, Buon Ma Thuot 630000, Vietnam, e-mail: phantuquy@ttn.edu.vn

Thanh Q. Bui: Department of Chemistry, University of Sciences, Hue University, Hue City 530000, Vietnam, e-mail: thanh.bui@hueuni.edu.vn **Nguyen Minh Thai:** Faculty of Pharmacy, University of Medicine and Pharmacy at Ho Chi Minh City, Ho Chi Minh City 700000, Vietnam, e-mail: minhthai2511@ump.edu.vn

Ly Nguyen Hai Du: Faculty of Pharmacy, University of Medicine and Pharmacy at Ho Chi Minh City, Ho Chi Minh City 700000, Vietnam, e-mail: haidu@ump.edu.vn

Nguyen Thanh Triet: Faculty of Traditional Medicine, University of Medicine and Pharmacy at Ho Chi Minh City, Ho Chi Minh City 700000, Vietnam, e-mail: nguyenthanhtriet1702@ump.edu.vn

Tran Van Chen: Faculty of Traditional Medicine, University of Medicine and Pharmacy at Ho Chi Minh City, Ho Chi Minh City 700000, Vietnam, e-mail: tvchenpharma@ump.edu.vn

Nguyen Vinh Phu: Faculty of Basic Sciences, University of Medicine and Pharmacy, Hue University, Hue 53000, Vietnam, e-mail: nvphu.dhyd@hueuni.edu.vn

Duong Tuan Quang: Department of Chemistry, University of Education, Hue University, Hue City 530000, Vietnam, e-mail: dtquang@hueuni.edu.vn **Dao-Cuong To:** Phenikaa University Nano Institute (PHENA), Phenikaa University, Yen Nghia, Ha Dong District, Hanoi 12116, Vietnam, e-mail: cuong.todao@phenikaa-uni.edu.vn

docking simulation, physicochemical analysis, and absorption, distribution, metabolism, excretion, and toxicity (ADMET) was designed for the theoretical argument on the potentiality of oilbased components (1-27) against H5 hemagglutinin in influenza A virus (PDB-5E32), wild-variant SARS-CoV-2 main protease (PDB-6LU7), and SARS-CoV-2 Omicron spike protein (PDB-7T9J). Theoretical arguments based on various computational platforms specify the most promising bio-inhibitors, i.e. 23 (biocompatibility: ground energy -966.73 a.u., dipole moment 3.708 Debye; bio-inhibitability: DS −12.5 kcal mol⁻¹; drug-likeness: mass 304.7 amu, log P 1.31; polar-interactability: polarizability 32.8 Å³) and **26** (bio-compatibility: ground energy -1393.66109 a.u., dipole moment 5.087 Debye; bio-inhibitability: DS -11.9 kcal mol⁻¹; drug-likeness: mass 437.5 amu, $\log P$ 4.28; polar-interactability: polarizability 45.7 Å³). The pkCSM-ADMET model confirms their favorable pharmacokinetics and pharmacology. The total essence is unsuitable for use as an antiviral source in its pure form since the most bioactive candidates are accountable for the small content. Particularly, **23** (7β-hydroxydehydroepiandrosterone) and 26 (ethyl cholate) are recommended for further experimental efforts of isolation and bioassaying trials.

Keywords: Curcuma sahuynhensis, antiviral activities, composition, in silico

ORCID: Phan Tu Quy 0000-0002-5986-5944; Thanh Q. Bui 0000-0003-4076-4323; Nguyen Minh Thai 0000-0002-8967-1753; Ly Nguyen Hai Du 0000-0001-5785-4435; Nguyen Thanh Triet 0000-0001-6710-2448; Tran Van Chen 0000-0003-1430-231X; Nguyen Vinh Phu 0000-0003-2389-3422; Duong Tuan Quang 0000-0002-4926-0271; Dao-Cuong To 0009-0001-2954-8702; Nguyen Thi Ai Nhung 0000-0002-5828-7898

1 Introduction

Curcuma L. is one of the largest genera of the ginger family, Zingiberaceae, with approximately 130 recognized species (https:// powo.science.kew.org/taxon/urn:lsid:ipni.org:names:331178-2, April 2023, Accessed: 12.04.2023). These rhizomatous herbaceous perennials are widely distributed in tropical and subtropical regions, especially in South-to-Southeast Asia and Northern Australia. In Vietnam, 28 Curcuma species have been previously scientifically described [1] with some morphological similarities, e.g., few-flowered cone-like inflorescence, congested bracts, straight trunk, and spurred anthers [2]. Besides being delightful ornamental plants, members of the Curcuma genus are well known for being an essential source of flavoring agents and cosmetics in Asian cultures [3]. According to folk experience, they are known for various pharmacological properties, e.g., antioxidant, anti-inflammatory, antiproliferative, antimicrobial, hypotensive, hypoglycemic, hepatoprotective, and neuroprotective activities. Curcuma longa (turmeric) and Curcuma zedoaria (zedoary) are the most extensively investigated species due to their great commercial value [4]. Nevertheless, other Curcuma species have been studied to a narrower extent.

Curcuma sahuynhensis Škorničk. & N.S. Lý is an endemic species in Curcuma subgenus Ecomatae, which was first discovered and described in 2015 in Quang Ngai Province, Vietnam [5]. Its morphological characteristics with all parts of the plants are shown in Figure 1. This rhizomatous herb has a void to narrowly ovoid and slightly aromatic rhizomes. Mature plants can reach 80 cm in height, with up to 10 leaves in ovate-to-elliptic shapes. Its flowers typically bloom from

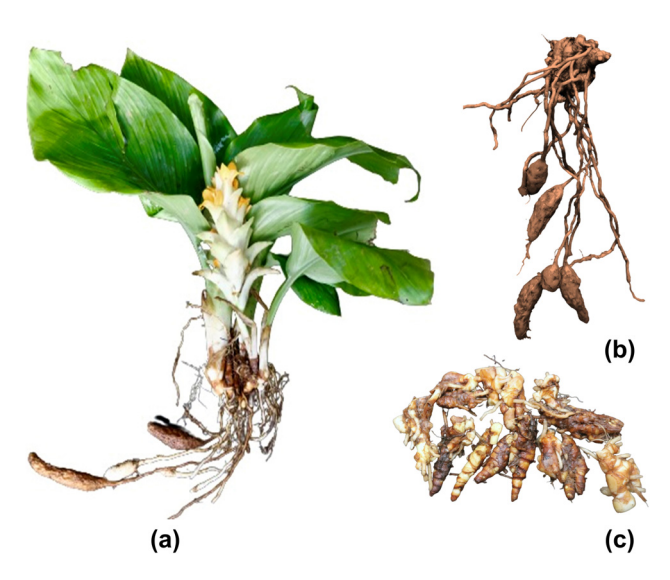


Figure 1: *Curcuma sahuynhensis* morphology: (a) full body, (b) roots, and (c) rhizome.

August to October annually. Generally, C. sahuynhensis shares several similar morphological traits to some other subgenus Ecomatae in Vietnam, namely Curcuma newmanii, Curcuma singularis, and Curcuma xanthella. Inflorescences of the herb are often harvested as vegetables for a meal by resident people [5]. To the best of our knowledge, since the time of the first description (2015), there have been only two reports on chemical and biological characteristics. In 2020, Sam et al. presented the first phytochemical analysis and bioactivity screening of C. sahuynhensis, which revealed its activity against a variety of gram-positive bacteria (Enterococcus faecalis, Staphylococcus aureus, and Bacillus cereus) and a pathogenic yeast (Candida albicans) [6]. More recently, in 2022, Van Chen et al. [7] published a paper on macro- and micro-morphological features, physicochemical parameters, phytoconstituents, and powder characteristics of the herbs. The authors also carried out a preliminary pharmacognostic screening by comparing the detected phytochemicals with the bioactivities of those already known to the literature; yet, no concrete evidence was established. Despite its local popularity and promising bioactivity, the potentiality of C. sahuynhensis is still vastly untouched by scientific communities, probably because of its highly regional endemics (only in Quang Ngai province, Vietnam). Therefore, more efforts, especially on the phytochemical-activity relationship, are required to allocate better the biological potential, thus reasoning further pre-clinical attempts. However, conventional trial-and-error lab-based tests are considered cost- and time-ineffective given the bio-versatility of natural products.

Regarding general bioactivity, natural essential oils are often classified into four groups based on their structure: monoterpenes, oxygenated terpenes, terpene esters, and sesquiterpenes. Typically, these substances have significant biological activity, especially antiviral potentiality. The most prominent essential oil constituent is monoterpenes obtained by liquid extraction and steam distillation of edible and medicinal plants [8]. Many research attempts have demonstrated that monoterpenes exhibit antibacterial, antiviral, and antifungal properties. For example, Eucalyptus oil and its active component, 1,8-cineole, were reported to possess in vitro antiviral activities against various strains of viruses, including enveloped mumps viruses (MV) and herpes simplex viruses (HSV-1 and HSV-2) [9]. Recently, β-caryophyllene, a sesquiterpene, was found as the major compound of essential oil from Lippia alba and demonstrated for its antiviral activity against Zika virus (ZIKV) in vitro and in silico [10]. In terms of diterpenes, many candidates have been shown to have antiviral activity, including kirkinine, excoecariatoxin (anti-HIV) [11], jiadifenoic acids (anti-Coxsackie virus) [12], briaexcavatolide U, and briaexcavatin L (anti-HCMV) [13]. Certainly, this review

is far from complete, indicating the enormous potential of natural essential oils in general for their antiviral activities and those extracted from *C. sahuynhensis* in particular.

Over the last few years, the outbreaks of dangerous viral infections have raised serious concerns as they are causing pandemics on a worldwide scale and pressuring the global healthcare systems. This means searching for demotic and editable sources with antiviral activities is necessary as food-and-drug recommendations for daily use as supplements to improve public health. Typically, the most prevalent diseases include those caused by influenza and SARS (recently, SARS-CoV-2) viruses. The former includes three types, named A, B, and C types, which cause respiratory illness with flu-like symptoms. Patients infected with influenza types A and B often face more serious-to-fatal complications. The influenza virus designation refers to the two components that envelope the virus's surface, hemagglutinin (HA) [14] and neuraminidase (NA) [15]. HA protein is required for the virus to attach to the glycoprotein or glycolipid in the host cell membrane through multivalent connections to sialoglycans, enabling the propagation of freshly manufactured virus inside the host. Hence, this structure is considered a high-potential target for bioactive inhibition by halting the intrusion. NA protein is a glycoside hydrolase enzyme required for viral replication. In the case of SARS-2 viruses, the effects have been prevalently recognized over the last 3 years from the views of both healthcare and the economy. Shortly after the first breakout, the genome of CoV was found to encode two proteins, designated as PPLA and PPLB [16], involving infection, replication, and polymerase activities [17]. The polyprotein is synthesized after transcription/translation steps and is then proteolyzed to yield nonstructural proteins. Two cysteine proteases, e.g. Papain-like protease and 3-chymotrypsin-like protease (also known as Mpro), mediate proteolytic processing. By mechanism, effective Mpro inhibitors might prevent viral replication [18], thus considered the most appealing target for SARS-CoV-2 treatments. Concerning its mutability, Omicron variants include over 50 mutations, at least 30 of those located in the spike protein. This protein is composed of two subunits, i.e. S1 and S2, particularly essential for viral adhesion to host cells, and the second is responsible for virus-cell membrane fusion [19,20]. From clinical observations, not only the increase of transmissibility and virulence but also the reduction of vaccination efficacy was reported relating to the infection of Omicron variants. This means that the protein structure is also

By harnessing computer-based power, in silico research can compensate for the cost and time disadvantages of labbased experimental trials to quickly allocate the most promising biological candidates. In fact, the applicability of

computational chemistry has been seen extensively in a broad range of bio-physico-chemical aspects, such as virology [21], oncology [22], neurology [23], or the development of drug-delivery nanocarriers [24]. With the appropriate combination of the views from different computational platforms, the theoretical analysis can provide more reliable predictions and, thus, results with higher accuracy. For example, the electronic properties of a chemical structure, e.g., electronic stability, dipole moment, and potential distribution, can be obtained from an ab initio calculation, which in turn can be used for argument on intermolecular interactability. Besides, molecular docking simulation is a useful technique often exploited for the prediction of ligand-protein inhibitability based on the interacting conformation of a potential inhibitor and selective sites [25]. Most algorithms are simply based on the static pseudo-Gibbs free energy between the two participants [26], giving them the light-duty leads; on the other side, the pre-docking conditions, representing physio-chemical resistance, are often omitted. Fortunately, this downside can be solved by the incorporation of other computational platforms, e.g. statistically regressive models, to retrieve the missing physicochemical effects. Similarly, the pharmacokinetics and pharmacological properties of a promising phytochemical can be predictable using available special-purpose regressive models, e.g. SwissADME. These computational implementations, coupled with consistent arguments, can screen a large number of compounds for their potentiality on both biological compatibility and pharmacological suitability.

In this work, a variety of in silico platforms was used in combination to predict the antiviral activities of the phytochemicals in C. sahuynhensis rhizome n-hexane fraction. The input for the computational implementations was the data collected from experiments. The biological targets were important protein structures of the influenza virus and SARS-CoV-2. Currently, there is little knowledge on C. sahuynhensis collected in the literature; therefore, the results can serve as the justification for more selective attempts to exploit the natural source.

2 Materials and methods

2.1 Experiment

2.1.1 Plant material

Fresh rhizomes of C. sahuynhensis were collected from Quang Ngai Province, Vietnam (Figure 1). The scientific name of the plant was identified by Dr. Nguyen Thanh Triet. The study sample was profiled by DNA-based identification and approved as the public database by GenBank under the code OM021341.1 (https://www.ncbi.nlm.nih.gov/nuccore/2170415927, April 2023, Accessed: 12.04.2023). A voucher specimen (sample code: CS-11.21) was deposited at the Laboratory of Traditional Medicine, Faculty of Traditional Medicine, University of Medicine and Pharmacy at Ho Chi Minh City.

2.1.2 Chemical extraction

After harvesting, the rhizomes were soil-removed, washed and dried at room temperature, and ground into middlings before being subjected to chemical extraction. Powdered rhizomes of C. sahuynhensis (300 g) were under percolation-based extraction with ethanol (96%), yielding a total extract. The solvent was removed by a rotary evaporator at $45 \pm 2^{\circ}C$, leaving a crude extract. The crude extract was under liquid–liquid distribution with n-hexane to obtain respective fractional extracts. The n-hexane fraction was preserved at low temperatures (4°C).

2.1.3 Gas chromatography-mass spectrometry (GC-MS)

The chemical constituents of *C. sahuynhensis* rhizome *n*-hexane fraction were identified using GC-MS: Agilent GC 7890B-MS 5975C instrument coupled with a DB-5MS column (30 m \times 0.25 mm \times 0.25 µm). The *n*-hexane fraction 1.0 (µL) was injected into the GC column with a 20:1 split ratio; GC temperature program: (i) initiating at 70°C for 1 min (for isothermal condition); (ii) increasing linearly to 300°C at the rate of 20°C min⁻¹ (for 20 min) with the inlet temperature set at 250°C; MS configurations: MS transfer line temperature and ion source temperature with 230°C; EI mode with 70 eV ionization voltage; sector mass analyzer scan from 29 to 650 amu. Helium was used as the carrier gas with a constant flow rate of 1.2 mL min⁻¹. NIST-17 database was used as the standard spectral reference.

2.2 Computation

2.2.1 Quantum calculation

Density functional theory (DFT) was used for the calculation of molecular quantum properties. Software used were Gaussian 09 for calculation and GaussView 05 for visual

rendering. Configurations used were no symmetry constraints [27]; functional M052X and basis set 6-311++g(d,p) for geometrical optimization [28,29]; functional M052X and basis set def2-TZVPP for molecular electrostatic potential (MEP) calculation; and imaginary frequency check for non-transitional state. Approximations were frozen-core method and resolution-of-identity technique. Termination was self-consistent field convergence at 10^{-8} a.u.; integration grid "m4."

2.2.2 Docking simulation

The molecular docking technique was used for the simulation of ligand–protein static interaction. MOE 2015.10 software was used [30]. The procedure is as follows: input, docking, checking, and interpretation.

- (i) Input preparation: Crystal structures of H5 HA in influenza A virus (PDB-5E32; DOI: 10.2210/pdb5E32/ pdb, April 2023, Accessed: 12.04.2023), wild-variant SARS-CoV-2 main protease (PDB-6LU7; DOI: 10.2210/ pdb6LU7/pdb, April 2023, Accessed: 12.04.2023), and SARS-CoV-2 Omicron spike protein (PDB-7T9J; DOI: 10.2210/pdb7T9J/pdb, April 2023, Accessed: 12.04.2023) were downloaded from RCSB Protein Data Bank; configurations: 4.5 Å for active grid, MMFF94x force field. Chemical formulae for ligands were identified by GC-MS in this work; configuration: Conj Grad optimization, Gasteiger-Huckel charge assignment.
- (ii) Docking simulation: The interaction between the selected ligand and its targeted protein was run by MOE 2015.10.
- (iii) Checking iteration: The simulated participants (protein and ligand) were allowed for a re-docking implementation to check the root-mean-square deviation (RMSD) value of the backbone atoms. The value under 2 Å is understood as a reliable result.
- (iv) Theoretical interpretation: The results include 2D interaction maps, 3D conformational visualization, and other inhibitory parameters (docking score [DS] energy, RMSD value, and counts of binding bonds). In particular, DS energy is often interpreted as the pseudo-Gibbs free energy, i.e., the formation energy of the associated ligand–protein complex, thus considered as primary parameters for inhibitory effectiveness.

Figure 2 presents the input for ligands in this work; the structural formulae were from the experiments, i.e., extraction and GC-MS. Figure 3 shows the crystal assemblies of the protein used in this work and the control drugs; the data were referenced from RCSB-Protein Data Bank.

Figure 2: The structural formula of bioactive volatile compounds (1–27) in *Curcuma sahuynhensis* rhizome *n*-hexane extract.

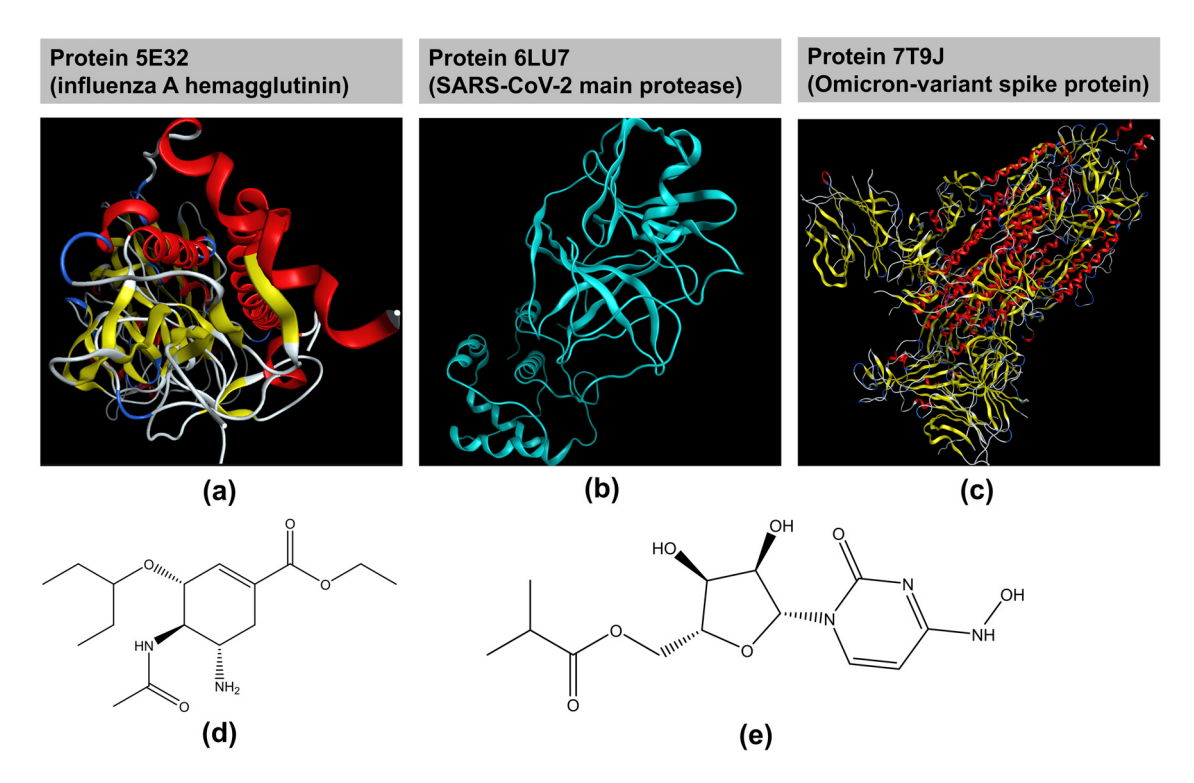


Figure 3: Biological assembly of (a) influenza A HA 5E32, (b) SARS-CoV-2 main protease 6LU7, (c) Omicron-variant spike protein 7T9J; structural formula of (d) Oseltamivir **D1**, (e) Molnupiravir **D2**.

Table 1: Curcuma sahuynhensis oil-based volatile bioactive components identified by GC-MS

Notation	Retention time (min)	Nomenclature	Formula	Area (%)	Class
1	3.84	1,8-Cineole	C ₁₀ H ₁₈ O	1.17	Om
2	4.82	Camphor	$C_{10}H_{16}O$	0.49	Om
3	6.42	Geranyl acetate	$C_{12}H_{20}O_2$	2.42	Om
4	6.52	Ylangene	$C_{15}H_{24}$	0.56	Sh
5	6.85	Caryophyllene	$C_{15}H_{24}$	0.45	Sh
6	7.10	Humulene	$C_{15}H_{24}$	0.51	Sh
7	7.18	Cubebol	$C_{15}H_{26}O$	0.43	Os
8	7.25	4-Ethylphenetole	$C_{10}H_{14}O$	0.48	Ah
9	7.32	β-Selinene	$C_{15}H_{24}$	1.21	Sh
10	7.93	Caryophyllen oxide	$C_{15}H_{24}O$	2.82	Os
11	8.10	Humulene oxide II	$C_{15}H_{24}O$	3.82	Os
12	8.75	Cis-Z-α-bisabolene epoxide	$C_{15}H_{24}O$	1.70	Os
13	9.23	Ambrial	$C_{16}H_{26}O$	3.79	Os
14	9.70	Methyl palmitate	$C_{17}H_{34}O_2$	11.77	Ae
15	9.88	3-Deoxyestradiol	$C_{18}H_{24}O$	1.98	St
16	10.05	Ethyl palmitate	$C_{18}H_{36}O_2$	6.18	Ae
17	10.15	(E)-15,16-Dinorlabda-8(17),11-dien-13-one	$C_{18}H_{28}O$	1.51	Os
18	10.56	Methyl linoleate	$C_{19}H_{34}O_2$	9.03	Ae
19	10.59	Linoleoyl chloride	C ₁₈ H ₃₁ CIO	2.87	Ha
20	10.71	Methyl isostearate	$C_{19}H_{38}O_2$	1.95	Ae
21	10.88	Ethyl linoleate	$C_{20}H_{36}O_2$	4.26	Ae
22	10.90	Ethyl oleate	$C_{20}H_{38}O_2$	1.37	Ae
23	11.32	7β-Hydroxydehydroepiandrosterone	$C_{19}H_{28}O_3$	2.05	St
24	11.92	(<i>E</i>)-Labda-8(17),12-diene-15,16-dial	$C_{20}H_{30}O_2$	2.04	Od
25	13.16	Villosin	$C_{20}H_{28}O_2$	2.54	Os
26	13.20	Ethyl cholate	$C_{26}H_{44}O_5$	1.46	As
27	13.77	Squalene	$C_{30}H_{50}$	2.36	Tr

Om: oxygenated monoterpenes; Sh: sesquiterpene hydrocarbons; Os: oxygenated sesquiterpenes; Od: oxygenated diterpenes; Ae: aliphatic ester; As: aliphatic steroid ester; Ah: aroma hydrocarbons; Ha: halogenated aliphatic; Tr: triterpenes; St: steroids.

Figure 4: Geometrically optimized structures of 1–27 by DFT at the level of theory M052X/6-311++g(d,p); unit of bond length: Å, unit of bond angle: °.

2.2.3 QSARIS analysis

The physical properties of each candidate were obtained from the QSARIS system (using the Gasteiger–Marsili method [31]) and compared to Lipinski's rule of five [32] for drug-like assessment. Parameters used were as follows: mass (amu), polarizability (ų), size (Å), and dispersion coefficients (log P and log S). Criteria were as follows: (i) mass <500 amu, (ii) hydrogen-donating groups ≤5, (iii) hydrogen-accepting groups ≤10, and (iv) log P < +5 [33,34].

2.2.4 Absorption, distribution, metabolism, excretion, and toxicity (ADMET) analysis

The pharmacokinetic properties of each candidate were obtained from SwissADME (http://www.swissadme.ch/, April 2023, Accessed: 12.04.2023), an ADMET predictor developed by Swiss Institute of Bioinformatics. Parameters were as follows: properties regarding ADMET. References were as follows: the theoretical interpretations and thresholds proposed by Pires et al. [35].

3 Results and discussion

3.1 Chemical composition of *n*-hexane fraction

Table 1 summarizes major volatile bioactive compounds in the n-hexane fraction of C. sahuynhensis rhizomes identified by GC-MS and their notation used in this report. In this screening stage, the standards of found compounds were not used for exact quantitative measurement; instead, the peak areas were addressed as a preliminary discussion on their contents. In total, there are 27 components detected. In particular, methyl palmitate (14; peak area 11.77%), methyl linoleate (18; peak area 9.03%), ethyl palmitate (16; 6.18%), ethyl linoleate (21; 4.26 peak area %), humulene oxide II (11; peak area 3.82%), and ambrial (13; peak area 3.79%) appear to be present as the components with significant amount. They likely comprise the major proportion of the essence, thus of special interest, thanks to their bioavailability. More generally, most compounds register the area values ca. 1–3%, likely accounting for the minor portions, and can be considered for isolation and application if predicted valuable enough. Otherwise, the constituents with likely negligible percentages (peak areas <1%) either hold low contributions to the total effect of the essential oil or are not deserved for cumulative enrichment from the economic standpoint. On the other hand, those with both promising bio-activities and potential bio-availability should be subjected to quantitative evaluation to measure the actual concentrations and validate their portions in the total essence.

In general, the major compounds detected in *C. sahuynhensis* essential oil have been demonstrated with diverse bio-active properties by other works. Methyl palmitate has been reported to have anti-inflammatory [36], anti-arthritic [37], acaricidal [38], antioxidant, insecticide, hemolytic, and hypocholesterolemic [39,40] properties. Ethyl palmitate has been determined to have anti-inflammatory, antioxidant, anti-androgenic, hemolytic, hypocholesterolemic, and antimicrobial activities [36,39,41]. Methyl linoleate has been identified as a bioactive anti-adipogenic [42] and anti-melanogenesis agent [43]. Ethyl linoleate has been proven to exhibit anti-inflammatory, antioxidant, and anti-acne activities [44–46]. Transparently, this review is incomplete; yet, the compounds are unlikely to be characterized by antiviral properties. This means that the activities against viruses (if

Table 2: Ground state electronic energy and dipole moment value of **1–27** by DFT at the level of theory M052X/6-311++q(d,p)

Compound	Ground state electronic energy (a.u.)	Dipole moment (Debye)
1	-467.20520	1.599
2	-465.99684	3.396
3	-619.83335	2.725
4	-586.10133	0.270
5	-584.82540	0.793
6	-546.74175	0.726
7	-662.56579	1.648
8	-464.77256	1.461
9	-586.11398	0.755
10	-661.29785	2.474
11	-661.29758	2.210
12	-661.30265	1.910
13	-700.67324	3.420
14	-818.86658	2.184
15	-775.73643	1.157
16	-858.18817	2.334
17	-778.09419	2.769
18	-895.04547	2.155
19	-1240.09215	3.565
20	-897.50357	2.135
21	-934.36698	2.306
22	-935.58736	2.336
23	-966.72618	3.708
24	-930.74548	4.262
25	-929.55614	5.139
26	-1393.66109	5.087
27	-1173.36492	0.354

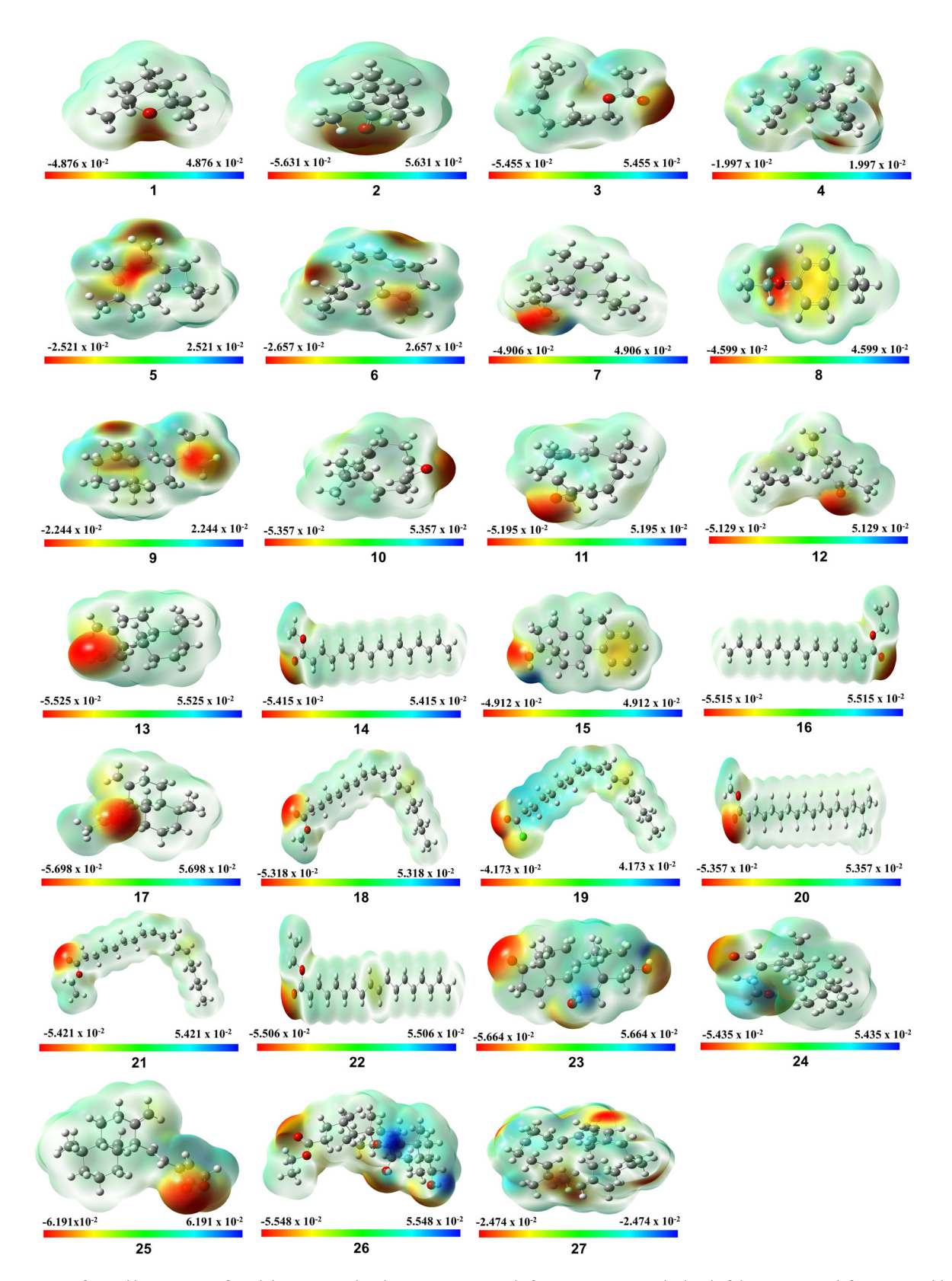


Figure 5: MEP formed by mapping of total density over the electrostatic potential of 1–27 using DFT at the level of theory M052X/def2-TZVPP; reddish region: negative electrostatic potential, bluish region: positive electrostatic potential, greenish region: null electrostatic potential.

any) are more likely allocated to those with moderate proportions, thus conducive to applying bioactive versatile natural products. In order to evaluate the utility of *C. sahuynhensis* against influenza A virus (H5N1) and SARS-CoV-2, the composition of the essence is further subjected to more in-depth analysis using *in silico* approaches.

3.2 DFT-based quantum chemical properties

The quantum calculation retrievals are the energy-optimal geometries and electronic characteristics, which are utilized for argument on *ab initio* intermolecular interactability of the host molecule. It is noteworthy that this is the view from the intrinsic chemical properties of the potential ligands (1–27) without any reference to inhibited structures.

The most stable structural geometries are shown in Figure 4. Overall, no explicit molecular constraints or abnormality are observed regarding the bonding angles and lengths. These unconstraint properties implicate the confirmation of the stable existence of natural products, thus validating the spectroscopic characterization and structural elucidation. In other words, for example, the calculated bonding lengths are within the range of characteristic ones, such as 1.2–1.4 Å for C–O, ca. 1.1 Å for C–H, and ca. 1.3–1.5 Å for C–C; also, the aromatic ring is in planar.

Table 2 summarizes their corresponding molecular properties, including ground state energy and dipole moment. The former represents chemical inactivity, while the latter defines the positive-negative charge separation in a system. Their negative ground-state energy, especially **18–27** (under –900 a.u.), indicates electronic stability, thus unlikely sensitive to chemical reactions and likely conducive to non-chemical interactions, e.g. ligand-protein inhibition. Particularly, 26 (-1393.66 a.u.), 19 (-1240.09 a.u.), and 27 (-1173. 36 a.u.) register the values of significance. Given dipole moment values, 25 (5.139 Debye), 26 (5.087 Debye), 24 (4.262 Debye), 23 (3.708 Debye), and 19 (3.565 Debye) possess predominant values; meanwhile, the corresponding figure for 27 (0.354 Debye) is marginal. This means that although 27 is promising from the view of chemical inertia, the candidate is considered incompatible with a dipole-solvent environment, such as physio-chemical media. In the case of 2 (camphor), although it has favored dipole moment, its high ground energy means that the compound is likely to induce chemical reactions with the body, thus not recommended for applications as a bio-inhibitor. Therefore, the intrinsic quantum properties suggest the potential of 19 and 23-26 for biological applications in general and protein-inhibited interactions (based on van de Waals forces or ionic bonds [47]) in particular.

Figure 5 provides MEP maps over the molecular plane of each compound (1-27); this equals the distribution of chemical activities with color-coding scheme given in the figure caption. The visualization explicitly suggests the elevated flexibility of 23-27 when in a potential physical interaction with collided complex structures; the explanation can be argued based on their arbitrarily and consecutively shifting chemical tendencies over the molecular planes (observed by the rapid switch of color schemes). This would be conducive to inhibitory applications against complex structures, such as proteins. From this perspective, although possessing a rather simple molecular structure, 19 is ably performing flexibility to a certain degree. In contrast, the others (1-22) seem to be rather neutral in terms of electronic potential with a limited region for external interaction.

In summary, quantum analysis preliminarily specifies **23–26**, and **19** as the most promising bio-inhibitors based on their intrinsic electronic properties.

3.3 Docking-based inhibitability

The inhibitory potential of each candidate toward specific protein structures is assessed by the docking technique. This considers their potentiality in the context of the static interactions between the ligands (1–27) and their targeted proteins related to Influenza (5E32) and SARS-CoV-2 (6LU7 and 7T9J). Following this scope, the primary parameters selected to evaluate the inhibitory effectiveness are the total DS values, i.e., the representative of pseudo-Gibbs free energy of inhibitory complex formation, and the hydrogen-like bonds,

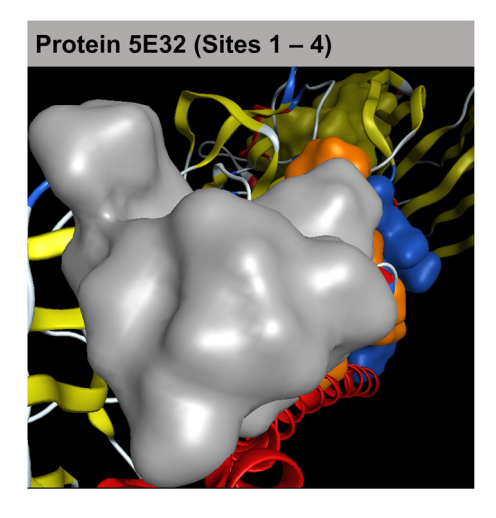


Figure 6: Quaternary structure of 5E32 with approachable sites by the ligands: site 1 (yellow), site 2 (blue), site 3 (grey), and site 4 (orange).

Table 3: Primary docking results on inhibitability of ligand-5E32 complexes

P	L	Site	1	Site	2	Site	3	Site	4	Average
		E	N	E	N	E	N	E	N	E
5E32	1	-9.1*	1*	-7.3	0	-7.0	0	-6.8	0	-7.6
	2	-8.9	1	-10.8*	2*	-8.6	1	-7.1	0	-8.9
	3	-8.7	1	-7.3	0	-10.5*	2*	-6.9	0	-8.4
	4	-7.0	0	-7.2*	0*	-6.7	0	-6.5	0	-6.9
	5	-7.1	0	-8.0*	0*	-7.0	0	-6.4	0	-7.1
	6	-7.0	0	-6.8	0	-6.5	0	-7.4*	0*	-6.9
	7	-8.7	1	-8.5	1	-7.0	0	-10.1*	2*	-8.6
	8	-10.3*	2*	-8.0	1	-6.4	0	-6.7	0	-7.9
	9	-7.3	0	−7.6 *	0*	-6.8	0	-6.2	0	-7.0
	10	-8.6	1	-8.2	1	-10.1*	2*	-7.9	0	-8.7
	11	-7.9	1	-7.0	0	-10.6*	2*	-6.4	0	-8.0
	12	-7.3	1	-6.7	0	-6.3	0	-10.8*	2*	-7.8
	13	-7.0	1	-6.6	1	-6.1	0	-10.6*	2*	-7.6
	14	-10.3*	2*	-7.3	1	-6.8	0	-7.0	1	-7.9
	15	-10.4	2	-11.9*	3*	-8.2	1	-8.0	1	-9.6
	16	-8.5	1	-8.1	1	-9.5*	2*	-7.7	0	-8.5
	17	-8.4	1	-7.2	0	-9.8*	2*	-7.1	0	-8.1
	18	-7.8	1	-8.0	1	-6.3	0	-9.6*	2*	-7.9
	19	-6.8	0	-8.9*	1*	-6.5	0	-6.7	0	-7.2
	20	-7.8	1	-8.0	1	-10.0*	2*	-7.4	0	-8.3
	21	-8.3	1	-7.4	0	-9.5*	2*	-6.9	0	-8.0
	22	-8.0	1	-7.7	1	-9.0*	2*	-6.8	0	-7.9
	23	-10.3	2	-8.8	1	-8.5	1	-12.9*	4*	-10.1
	24	-8.1	1	-8.0	1	-7.6	0	-12.0*	3*	-8.9
	25	-9.7*	2*	-8.4	1	-7.2	0	-6.9	0	-8.1
	26	-10.0	2	-9.8	2	-8.3	1	-12.1	4	-10.1
	27	-7.5	0	-8.0*	0*	-7.0	0	-7.1	0	-7.4
	D1	-12.4*	3*	-9.3	2	-8.5	1	-8.0	1	-9.6

P: protein; L: ligand; E: DS value (kcal mol⁻¹); N: number of hydrophilic interactions.

i.e. the representative of strong ligand-protein binding. In this discussion, the average DS value is reasoned as the representative indicator of a multi-site inhibitory process. In principle, a simultaneous inhibition is more likely to channel sufficient distortion forces onto the secondary-tertiary protein structures, which in turn induces the decreased efficacy of the enzymatic activities overall based on the mechanism of allosteric non-competitive inhibition. This approach is especially significant since the candidates are from natural sources with a diversity of structural elements and chemical characteristics.

For further reference, the in-detail data for each of the most effective inhibitory systems regarding each ligandprotein inhibition are provided in Supporting Information. The corresponding visualizations of in-site arrangements and interaction maps are presented in this report with a symbol-coding scheme given in the figure caption.

3.3.1 Protein 5E32

The sites of 5E32 with the highest vulnerability toward the ligands (1–27 and D1) are shown in Figure 6; meanwhile, the corresponding primary docking parameters are given in Table 3. In general, the testing compounds register different affinities toward the sites. The most effective inhibitors against 5E32 (influenza A HA) can be interpreted by the average DS values, ranked by the order: 23 \approx 26 (DS_{average} $-10.1 \text{ kcal mol}^{-1}$) > **15** \approx **D** (DS_{average} $-9.6 \text{ kcal mol}^{-1}$). These candidates are expected to perform equal-to-elevated efficacy compared to the commercialized drug oseltamivir in terms of the inhibitory mechanism. The average values are of importance as in-reality biological inhibition is a rather simultaneous process, i.e. multi-site inhibition, than a selective one against a specific site. Besides, 19 and 24 (DS_{average}

^{*}Most effective ligand-protein complexes (in-detail data provided in Supporting Information).

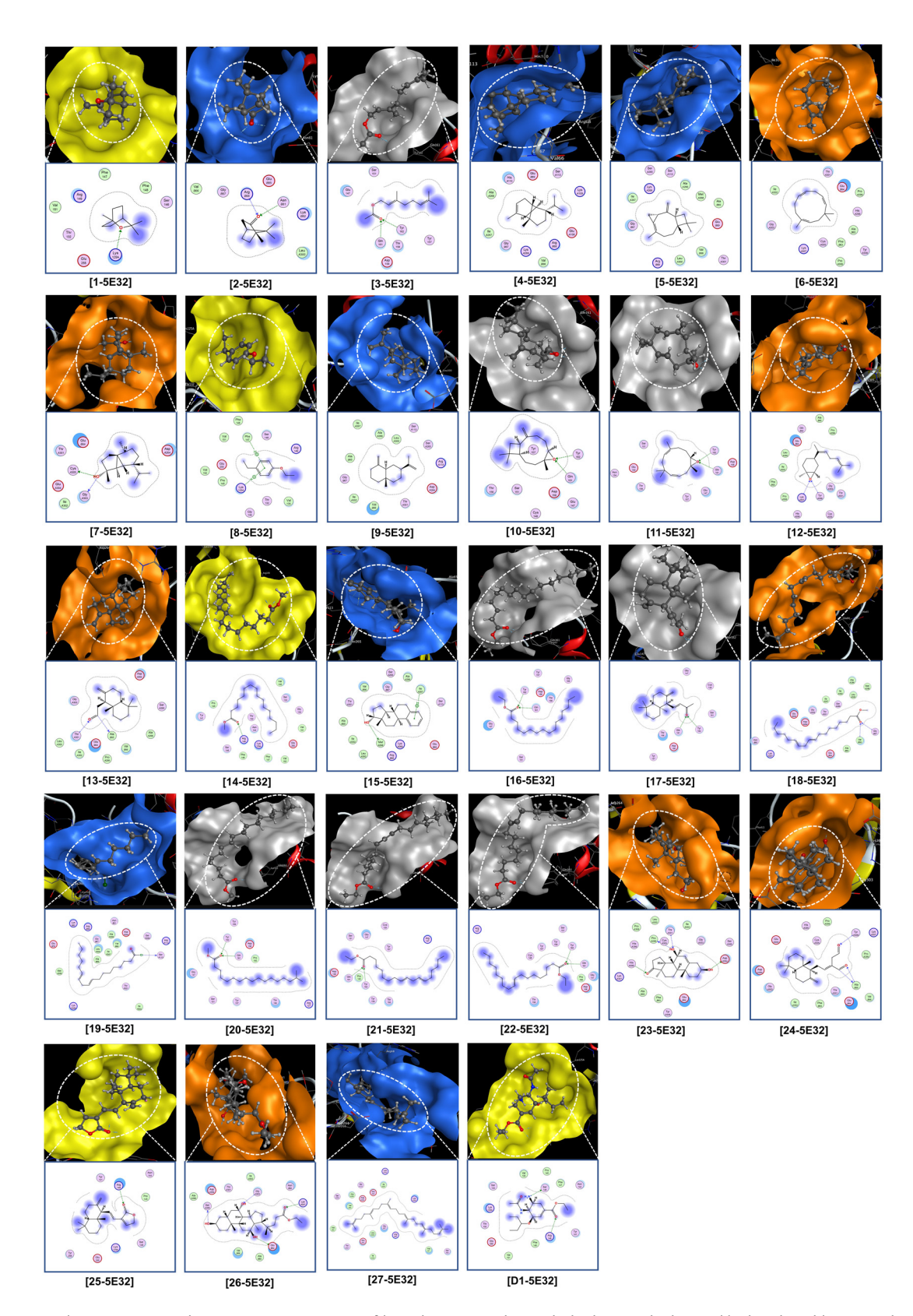


Figure 7: Visual presentation and in-pose interaction map of ligand-5E32 complexes; dashed arrow: hydrogen-like bonding, blurry purple: van der Waals interaction, dashed contour: conformational fitness.

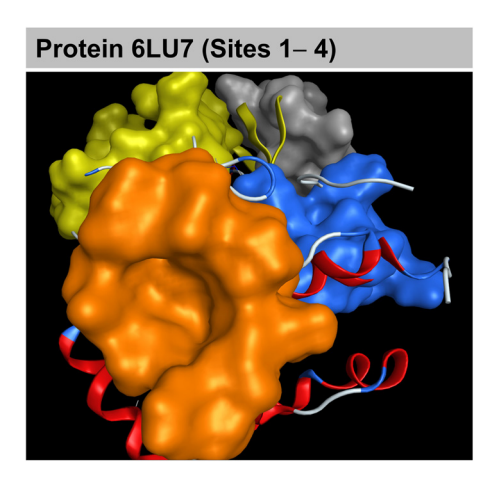


Figure 8: Quaternary structure of 6LU7 with approachable sites by the ligands: site 1 (yellow), site 2 (blue), site 3 (grey), and site 4 (orange).

 $-8.9~\rm kcal~mol^{-1}$) are also considerable. In contrast, although **25** and **27** are preceding suggested by their electronic properties (given by quantum analyses), in the context of ligand-5E32 inhibitability, they seem to be incompetent. If considering the most effective ones, the theoretical argument can also propose the ranking: **23-5E32** (DS $-12.9~\rm kcal~mol^{-1}$) > **D1-5E32** (DS $-12.4~\rm kcal~mol^{-1}$) > **26-5E32** (DS $-12.2~\rm kcal~mol^{-1}$) > **24-5E32** (DS $-12.0~\rm kcal~mol^{-1}$) > **15-5E32** (DS $-11.9~\rm kcal~mol^{-1}$); these can be thought of the main product of each ligand—protein inhibition.

Figure 7 presents in-site arrangements and interactive maps of the most effective ligand-5E32 inhibitory system. Given 3D in-pose morphology, the ligands rather fit tightly into the sites. This means further modification/functionalization of extended size is not recommended for current inhibitors. Regarding 2D interaction mapping, the ligands

Table 4: Primary docking results on inhibitability of ligand-6LU7 complexes

P	L	Site	1	Site	2	Site	3	Site	4	Average
		E	N	E	N	E	N	E	N	E
6LU7	1	-7.3	0	-7.0	0	-8.7*	1*	-6.8	0	-7.5
	2	-10.1*	2*	-8.9	1	-7.6	0	-7.1	0	-8.4
	3	-8.5	1	-11.2*	3*	-8.6	1	-8.2	1	-9.1
	4	−7.1*	0*	-6.8	0	-6.5	0	-6.2	0	-6.7
	5	-6.4	0	-6.8	0	-6.2	0	-7.0*	0*	-6.6
	6	-8.2*	1*	-7.0	0	-6.7	0	-6.1	0	-7.0
	7	-8.5	1	-9.7*	2*	-7.3	0	-6.9	0	-8.1
	8	-9.2*	2*	-8.1	1	-8.0	1	-7.4	0	-8.2
	9	-7.6	0	-8.8*	1*	-7.3	0	-7.0	0	-7.7
	10	-9.3*	2*	-8.4	1	-7.8	0	-7.3	0	-8.2
	11	-8.6	1	-9.0*	2*	-8.0	0	-7.5	0	-8.3
	12	-7.7	0	-7.4	0	-8.1*	1*	-7.2	0	-7.6
	13	-9.9*	2*	-8.0	1	-7.6	0	−7.1	0	-8.2
	14	-8.3	1	-9.7*	2*	-8.0	1	-7.7	0	-8.4
	15	-8.0	1	-11.4*	3*	-8.2	1	-7.9	1	-8.9
	16	-7.6	0	-8.4*	1*	-6.9	0	-6.5	0	-7.4
	17	-8.3*	1*	-7.2	0	-7.0	0	-6.8	0	-7.3
	18	-8.2	1	-9.7*	2*	-7.9	0	-7.4	1	-8.3
	19	-8.8	1	-9.6*	2*	-7.8	0	-7.6	0	-8.5
	20	-7.2	0	-9.3*	2*	-7.0	1	-6.7	0	-7.6
	21	-7.7	0	-8.2*	1*	-7.2	0	-6.4	0	-7.4
	22	-8.5	1	-11.8*	3*	-7.4	1	-7.0	0	-8.7
	23	-11.6*	3*	-8.8	1	-8.5	1	-7.8	0	-9.2
	24	-10.0*	2*	-9.0	1	-7.6	0	−7.1	0	-8.4
	25	-8.2	1	−11.9*	3*	-8.0	1	-7.7	0	-9.0
	26	-10.6	2	-10.3	2	-9.0	1	-12.4*	4*	-10.6
	27	-7.4	0	-8.9*	1*	-7.1	0	-6.8	0	-7.6
	D2	-12.0*	3*	-10.1	2	-8.5	1	-8.2	1	-9.7

P: protein; L: ligand; E: DS value (kcal mol⁻¹); N: number of hydrophilic interactions.

^{*}Most effective ligand-protein complexes (in-detail data provided in Supporting Information).

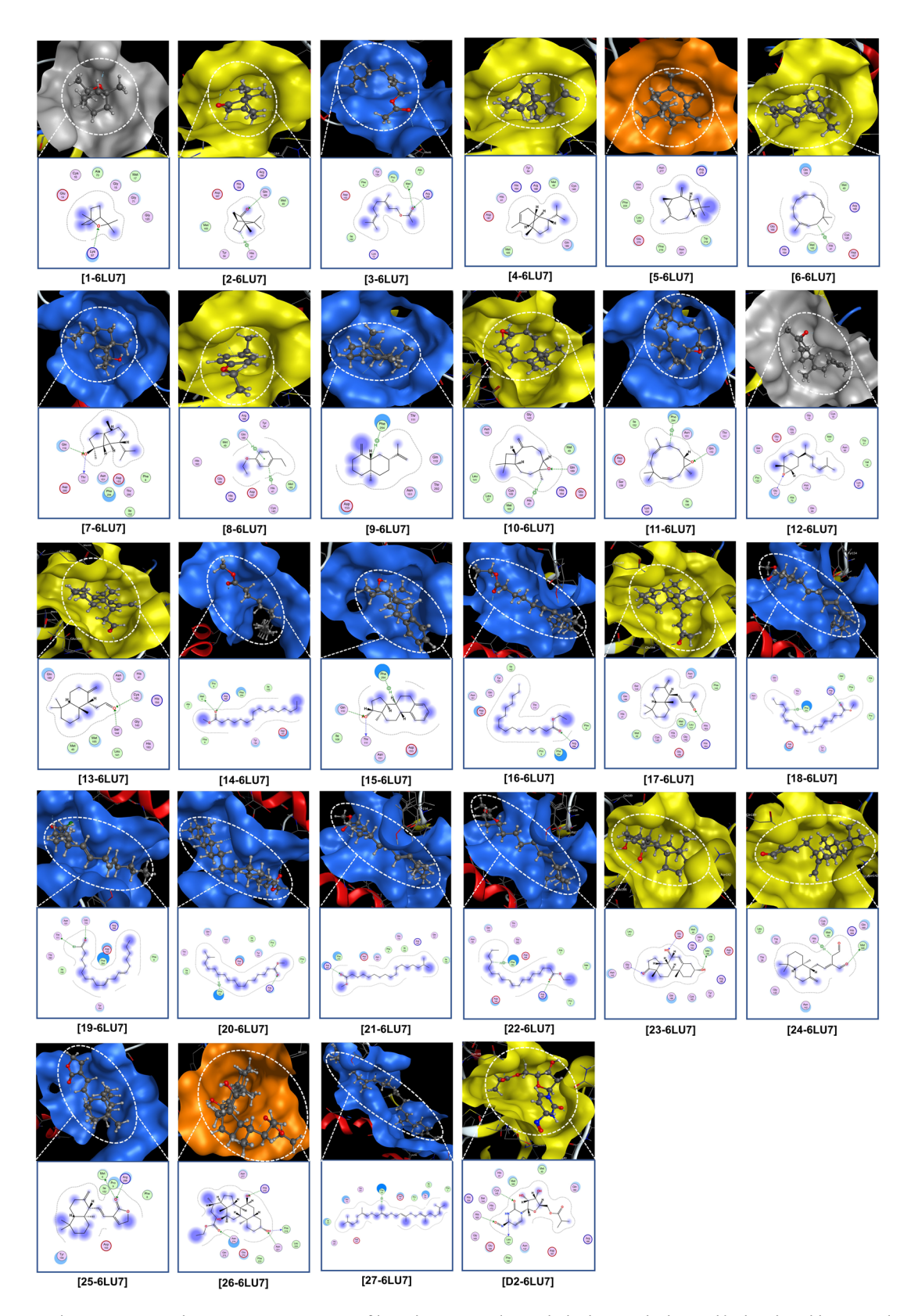


Figure 9: Visual presentation and in-pose interaction map of ligand-6LU7 complexes; dashed arrow: hydrogen-like bonding, blurry purple: van der Waals interaction, dashed contour: conformational fitness.

Table 5: Primary docking results on inhibitability of ligand-7T9J complexes

P	L	Site	1	Site	2	Site	3	Site	4	Average
		E	N	E	N	E	N	E	N	E
7T9J	1	-7.6	0	-7.3	0	-7.7	0	-8.7*	1*	-7.8
-	2	-8.4	1	-9.8*	2*	-8.1	1	-7.4	0	-8.4
	3	-8.6	1	-9.6*	2*	-7.0	0	-6.7	0	-8.0
	4	-8.3*	1*	-7.1	0	-6.8	0	-6.4	0	-7.2
	5	-6.9	0	−7.1*	0*	-6.3	0	-6.6	0	-6.7
	6	-8.2*	1*	-7.0	0	-7.2	0	-7.0	0	-7.4
	7	-8.0	1	-7.3	0	-7.2	0	-9.4*	2*	-8.0
	8	-9.2*	2*	-8.6	1	-7.6	0	-7.3	0	-8.2
	9	-8.5*	1*	-7.4	0	-7.0	0	-6.7	0	-7.4
	10	-11.6*	3*	-8.3	1	-8.0	1	-7.1	0	-8.8
	11	-10.3*	2*	-8.1	1	-7.8	0	-7.3	0	-8.4
	12	-8.5	1	-10.1*	2*	-8.2	1	-7.2	0	-8.5
	13	-8.7	1	-8.3	1	-10.0*	2*	-7.0	0	-8.5
	14	-9.9*	2*	-8.1	1	-7.0	0	-6.8	1	-8.0
	15	-9.7	2	-11.2*	3*	-8.5	1	-8.1	1	-9.4
	16	-8.2	1	-9.5*	2*	-7.6	0	-7.0	0	-8.1
	17	-8.4	1	-8.0	1	-9.1*	2*	-7.1	0	-8.2
	18	-10.2*	2*	-8.6	1	-7.3	0	-6.8	0	-8.2
	19	-8.7	1	-9.7*	2*	-8.5	1	-7.2	0	-8.5
	20	-8.3	1	-9.3*	2*	-7.0	0	-6.8	0	-7.9
	21	-8.0	1	-8.4	1	-10.4*	2*	-7.2	0	-8.5
	22	-8.3*	1*	-7.6	0	-7.2	0	-7.1	0	-7.6
	23	-10.8	2	-12.9*	4*	-10.3	2	-8.9	1	-10.7
	24	-10.6	2	-8.4	1	-12.7*	4*	-9.6	2	-10.3
	25	-8.5	1	-10.0*	2*	-7.6	0	-7.0	0	-8.3
	26	-9.9	2	-8.2	1	-11.2*	3*	-8.0	1	-9.3
	27	-6.5	0	-6.7	0	-6.2	0	−7.1*	0*	-6.6
	D2	-10.2	2	-10.9	2	-12.6*	4*	-8.7	1	-10.6

P: protein; L: ligand; E: DS value (kcal mol⁻¹); N: number of hydrophilic interactions.

have good conformational fitness with the in-site features given by the continuousness of dashed contours.

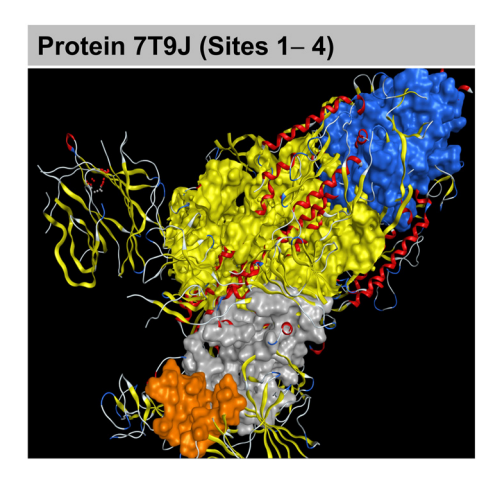


Figure 10: Quaternary structure of 7T9J with approachable sites by the ligands: site 1 (yellow), site 2 (blue), site 3 (grey), and site 4 (orange).

3.3.2 Protein 6LU7

The sites of 6LU7 with the highest vulnerability towards the ligands (1-27 and D2) are shown in Figure 8; meanwhile, the corresponding primary docking parameters are given in Table 4. Overall, the protein structure seems to be more susceptible to external inhibition at sites 1 and 2. On average, the most effective inhibitors against 6LU7 (SARS-CoV-2 main protease) are predicted in the order: **26** (DS_{average} -10.6 kcal mol⁻¹) > **D2** (DS_{average} -9.7 kcal mol⁻¹) > **23** (DS_{average} $-9.2 \text{ kcal mol}^{-1}$) > **3** \approx **25** (DS_{average} ca. -9 kcalmol⁻¹). Among these candidates, compound **26** is expected to perform elevated inhibitory ability, cf. the control drug; meanwhile, the others are still promising for further consideration. On the other hand, the corresponding figures for 19 and 24 (DS_{average} ca. -8.5 kcal mol⁻¹) can be considered yet not highly recommended; while **27** (DS_{average} ca. -7.6 kcal mol⁻¹) is rather incompetent, even though it is favored by certain quantum-based properties, i.e., ground energy and potential

^{*}Most effective ligand-protein complexes (in-detail data provided in Supporting Information).

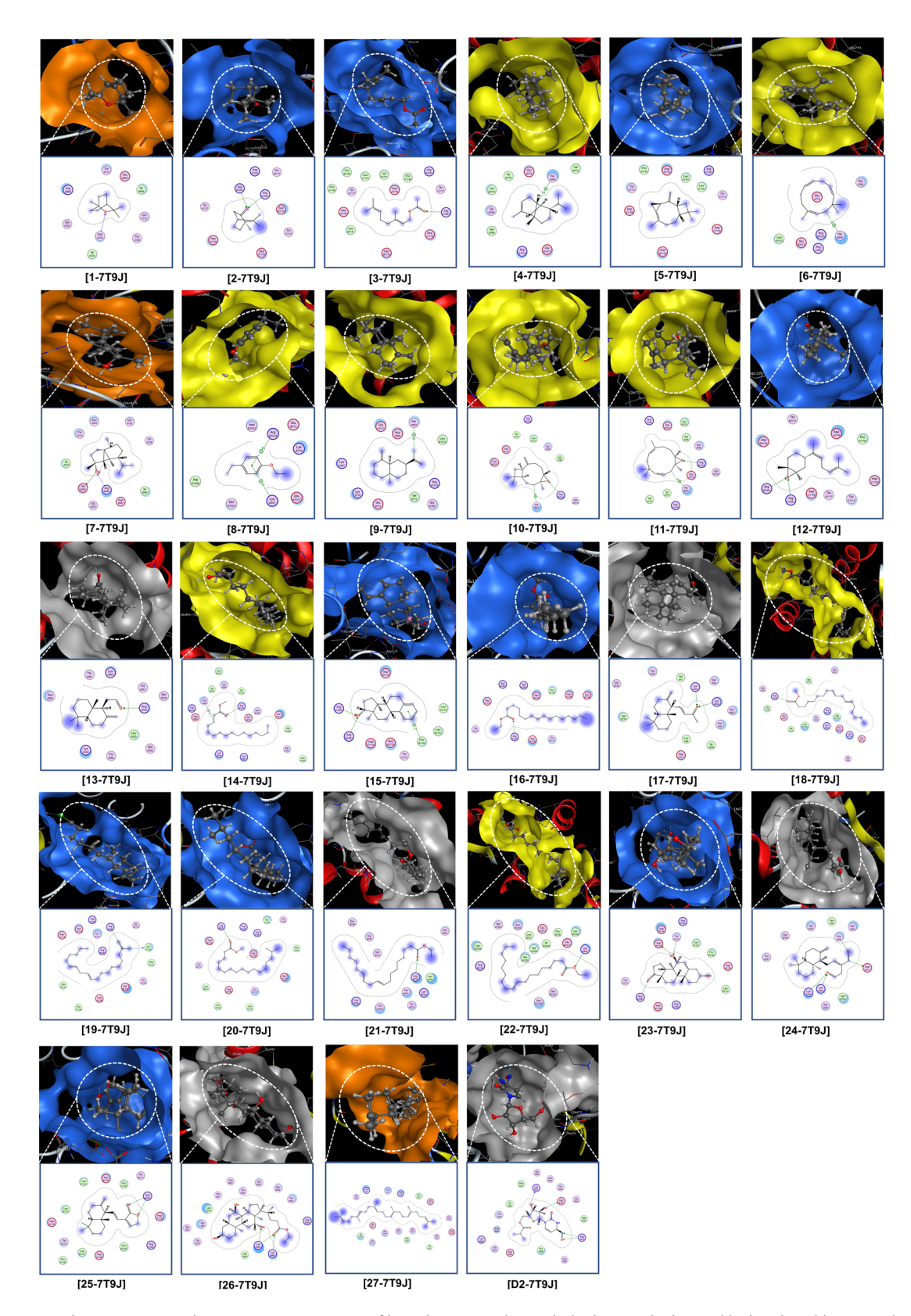


Figure 11: Visual presentation and in-pose interaction map of ligand-7T9J complexes; dashed arrow: hydrogen-like bonding, blurry purple: van der Waals interaction, dashed contour: conformational fitness.

Table 6: Physicochemical properties of 1-27 and D1-D2

Compound	$ar{ ext{DS}}$ (kcal mol $^{-1}$)	Mass	Polarizability (ų)	Volume (Å)	Dispersi	on coefficients	Hydrogen l	ond (5E32/6	LU7/7T9J)
		(amu)			log P	log S	H-acceptor	H-donor	Η-π
1	-8.8	154.7	17.6	280.2	2.45	-2.30	1/1/1	0/0/0	0/0/0
2	-10.2	153.2	18.0	257.5	2.10	-2.09	2/1/2	0/0/0	0/1/0
3	-10.4	196.9	22.3	360.9	3.21	-2.67	2/2/2	0/1/0	0/0/0
4	− 7.5	204.8	25.8	363.0	4.80	-4.47	0/0/0	0/0/0	0/0/1
5	-7.4	204.5	26.9	380.7	4.30	-4.27	0/0/0	0/0/0	0/0/0
6	-7.9	204.7	27.0	415.9	4.34	-4.80	0/0/0	0/0/0	0/1/1
7	-9.7	221.6	27.5	370.2	4.92	-4.11	0/1/1	2/1/1	0/0/0
8	-9.6	150.8	19.8	271.6	3.19	-2.78	0/0/0	0/0/0	1/2/1
9	-8.3	204.5	24.1	639.2	4.38	-4.62	0/0/0	0/0/0	0/1/1
10	-10.3	220.9	27.0	371.9	4.29	-4.10	2/1/2	0/0/0	0/1/1
11	-10.0	220.4	27.8	405.7	4.38	-4.03	2/1/1	0/0/0	0/1/1
12	-9.7	220.6	25.9	365.9	4.06	-4.17	2/1/2	0/0/0	0/0/0
13	-10.2	235.1	29.3	415.4	4.42	-4.06	1/2/2	1/0/0	0/0/0
14	-10.0	271.3	30.6	520.1	5.17	-4.32	2/1/1	0/1/0	0/0/1
15	-11.5	256.0	31.9	390.4	4.71	-4.26	0/1/2	1/1/0	2/1/1
16	-9.1	285.8	35.1	550.2	5.98	-5.07	2/1/2	0/0/0	0/0/0
17	-9.1	260.9	32.9	456.9	4.92	-4.25	2/1/2	0/0/0	0/0/0
18	-9.8	294.0	30.5	917.8	6.01	-4.87	2/1/2	0/0/0	0/1/0
19	-9.4	297.9	35.3	537.6	6.10	-5.03	0/1/1	1/1/1	0/0/0
20	-9.5	298.2	36.8	570.5	6.91	-5.12	2/1/2	0/0/0	0/1/0
21	-9.4	309.4	37.4	652.8	6.08	-5.24	2/1/2	0/0/0	0/0/0
22	-9.7	310.9	39.0	590.8	7.02	-5.15	2/2/1	0/0/0	0/1/0
23	-12.5	304.7	32.8	420.6	1.31	-2.48	2/2/3	2/1/1	0/0/0
24	-11.6	303.6	36.1	505.9	4.47	-4.15	2/0/3	1/1/1	0/1/0
25	-10.5	301.5	30.7	495.3	4.04	-4.13	2/2/2	0/1/0	0/0/0
26	-11.9	437.5	45.7	642.9	4.28	-4.89	2/3/3	2/1/0	0/0/0
27	-8.0	410.9	56.3	806.2	7.97	-6.93	0/0/0	0/0/0	0/1/0
D1	-12.3	312.3	32.4	480.8	1.41	-2.18	2/0/0	1/0/0	0/0/0
D2	-8.8	329.2	29.9	355.7	-1.43	-0.75	0/3/2	0/1/2	0/0/0

DS: average DS value calculated from all ligand-protein structures (ligand: 1-27 and D1-D2; protein: 5E32, 6LU7, 7T9]).

distribution. If considering the most effective ones, the theoretical argument can also propose the ranking: 26-6LU7 (DS $-12.4 \text{ kcal mol}^{-1}$) > **D2-6LU7** (DS $-12.0 \text{ kcal mol}^{-1}$) > **25-6LU7** \approx **22-6LU7** (DS -11.9 kcal mol⁻¹) > **23-6LU7** (DS -11.6 kcal mol⁻¹). In this consideration, 26 seems to have a special affinity toward site 3 of the protein structure.

Figure 9 presents in-site arrangements and interactive maps of the most effective ligand-6LU7 inhibitory system. First, 3D in-pose renderings reveal that the sites are still spacious after inhibited, thus implicating the potentiality of structural modification on the current ligands (if needed for compatible enhancement). Regarding 2D interaction mapping, the ligands are likely to have good conformational fitness with the in-site features given by the continuousness of dashed contours.

3.3.3 Protein 7T9J

The sites of 7T9J with the highest vulnerability toward the ligands (1-27 and D2) are shown in Figure 10; meanwhile, the corresponding primary docking parameters are given in Table 5. Overall, the protein structure is less selective for compatible inhibitors than that of the main protease. This might to some aspects explain the high transmission of Omicron variants by easily binding its spike proteins with external receptors. On average, the most effective inhibitors against 7T9J (Omicron-variant spike protein) are predicted in the order: 23 (DS_{average} -10.7 kcal mol⁻¹) > **D2** (DS_{average} -10.6 kcal mol⁻¹) > **24** (DS_{average} -10.3 kcal mol^{-1}) > **26** \approx **15** (DS_{average} ca. -9.4 kcal mol⁻¹). Again, **23**, **24**, and 26 are expected to be effective inhibitors against SARS-

Table 7: ADMET-based pharmacokinetics and pharmacology of 1-9

Property	1	2	3	4	5	6	7	8	9	Unit
Absorption										
Water solubility	-2.630	-2.895	-3.466	-5.705	-5.555	-5.191	-4.477	-2.663	-6.439	(1)
Caco2 permeability	1.485	1.499	1.627	1.374	1.423	1.421	1.454	1.658	1.429	(2)
Intestinal absorption	96.505	95.965	94.9	96.221	94.845	94.682	94.206	95.698	95.574	(3)
Skin Permeability	-2.437	-2.002	-1.665	-2.225	-1.58	-1.739	-2.238	-1.217	-1.702	(4)
P-glycoprotein substrate	Yes	No	No	No	No	Yes	No	No	No	(5)
P-glycoprotein I inhibitor	No	(5)								
P-glycoprotein II inhibitor	No	(5)								
Distribution										
VDss	0.491	0.331	0.103	0.806	0.652	0.505	0.466	0.346	0.639	(6)
Fraction unbound	0.553	0.459	0.395	0.115	0.263	0.347	0.183	0.307	0.089	(6)
BBB permeability	0.368	0.612	0.566	0.887	0.733	0.663	0.669	0.558	0.816	(7)
CNS permeability	-2.972	-2.158	-2.199	-1.659	-2.172	-2.555	-1.768	-1.859	-1.461	(8)
Metabolism										
CYP2D6 substrate	No	(5)								
CYP3A4 substrate	No	No	No	Yes	No	No	Yes	No	Yes	(5)
CYP1A2 inhibitor	No	No	No	Yes	No	No	No	Yes	Yes	(5)
CYP2C19 inhibitor	No	(5)								
CYP2C9 inhibitor	No	(5)								
CYP2D6 inhibitor	No	(5)								
CYP3A4 inhibitor	No	(5)								
Excretion										
Total Clearance	1.009	0.109	0.587	0.95	1.088	1.282	0.885	0.305	1.174	(9)
Renal OCT2 substrate	No	(5)								
Toxicity										
AMES toxicity	No	Yes	(5)							
Max. tolerated dose	0.553	0.473	0.474	-0.302	0.351	0.551	-0.340	0.832	-0.030	(10)
hERG I inhibitor	No	(5)								
hERG II inhibitor	No	(5)								
Oral Rat Acute Toxicity	2.010	1.653	1.683	1.644	1.617	1.766	1.877	1.829	1.581	(11)
Oral Rat Chronic Toxicity	2.029	1.981	2.272	1.356	1.416	1.336	1.458	2.094	1.511	(12)
Hepatotoxicity	No	(5)								
Skin Sensitization	Yes	Yes	Yes	No	Yes	Yes	Yes	Yes	Yes	(5)
T. Pyriformis toxicity	0.171	0.233	1.186	1.122	1.401	1.451	1.537	0.698	1.736	(13)
Minnow toxicity	1.735	1.458	0.604	0.128	0.504	0.716	0.69	0.920	0.078	(14)

⁽¹⁾ log mol L⁻¹; (2) log Papp (10⁻⁶ cm s⁻¹); (3) %; (4) log Kp; (5) Yes/No; (6) log L kg⁻¹; (7) log BB; (8) log PS; (9) log mL min⁻¹ kg⁻¹; (10) log mg kg⁻¹ day⁻¹; (11) log mg kg⁻¹ bw⁻¹ day⁻¹; (13) log μ g L⁻¹; (14) log mM.

related proteins, while **19** and **27** (DS_{average} > -8.5 kcal mol⁻¹) still present low reasoning for further consideration of development. Reducing this argument, the most effective inhibitory complexes are **23-779J** (DS -12.9 kcal mol⁻¹) > **24-779J** \approx **D2-779J** (DS -12.7 kcal mol⁻¹) > **10-779J** (DS -11.6 kcal mol⁻¹) > **26-779J** (DS -11.2 kcal mol⁻¹). This reinforces the potentiality of **23** as an inhibitor against 779J.

Figure 11 presents in-site arrangements and interactive maps of the most effective ligand-7T9J inhibitory system. Given 3D in-pose morphology, the sites are observed rather close and tight in space. This means further modification/functionalization to the ligands is not recommended. Regarding 2D interaction mapping, the ligand–protein conformational

fitness is seen at a high degree. This implies two opposite speculations: (i) it is difficult for the ligands to be placed inside the protein sites, yet (ii) the spatial bound might be conducive to the duration of effectiveness as the compounds are likely to be confined in the pose longer.

In summary, the results from the docking technique can only provide an early view of the static interactions between the candidates and their targeted proteins (at different sites). In order to validate the structure-denaturation aftereffects, molecular dynamics simulation can be used to directly monitor the motion/displacement of catalytic residues or experimental enzymatic bioassays can be carried out to examine the overall inhibitory efficacy.

Table 8: ADMET-based pharmacokinetics and pharmacology of 10-18

Property	10	11	12	13	14	15	16	17	18	Unit
Absorption										
Water solubility	-4.321	-4.162	-4.806	-5.729	-6.927	-4.904	-7.141	-5.684	-7.343	(1)
Caco2 permeability	1.414	1.515	1.519	1.513	1.601	1.663	1.596	1.451	1.612	(2)
Intestinal absorption	95.669	95.737	95.387	95.951	92.335	97.606	91.916	97.617	92.660	(3)
Skin Permeability	-3.061	-2.988	-3.333	-2.069	-2.595	-2.487	-2.682	-2.032	-2.719	(4)
P-glycoprotein substrate	No	Yes	No	(5)						
P-glycoprotein I inhibitor	No	(5)								
P-glycoprotein II inhibitor	No	Yes	(5)							
Distribution										
VDss	0.564	0.460	0.543	0.450	0.334	0.739	0.373	0.294	0.272	(6)
Fraction unbound	0.327	0.405	0.289	0.094	0.074	0.037	0.058	0.024	0.028	(6)
BBB permeability	0.647	0.669	0.689	0.688	0.749	0.294	0.759	0.681	0.767	(7)
CNS permeability	-2.521	-2.921	-2.410	-1.617	-1.678	-1.079	-1.777	-1.664	-1.463	(8)
Metabolism										
CYP2D6 substrate	No	(5)								
CYP3A4 substrate	No	No	No	Yes	Yes	Yes	Yes	Yes	Yes	(5)
CYP1A2 inhibitor	Yes	No	No	Yes	Yes	No	Yes	No	Yes	(5)
CYP2C19 inhibitor	Yes	No	Yes	Yes	No	Yes	No	No	No	(5)
CYP2C9 inhibitor	Yes	No	Yes	No	No	No	No	No	No	(5)
CYP2D6 inhibitor	No	(5)								
CYP3A4 inhibitor	No	(5)								
Excretion										
Total Clearance	0.905	1.065	1.225	1.035	1.861	1.074	1.912	1.128	2.032	(9)
Renal OCT2 substrate	No	(5)								
Toxicity										
AMES toxicity	No	Yes	No	(5)						
Max. tolerated dose	0.148	0.392	0.252	-0.451	0.178	-0.563	0.199	-0.201	-0.019	(10)
hERG I inhibitor	No	(5)								
hERG II inhibitor	No	(5)								
Oral rat acute toxicity	1.548	1.585	1.481	1.678	1.635	2.715	1.664	1.829	1.617	(11)
Oral rat chronic toxicity	1.224	1.161	1.191	1.207	2.998	1.423	3.019	1.156	3.004	(12)
Hepatotoxicity	No	No	No	No	No	Yes	No	Yes	No	(5)
Skin sensitization	Yes	(5)								
T. pyriformis toxicity	1.079	1.078	1.561	1.849	1.935	1.413	1.837	1.672	1.603	(13)
Minnow toxicity	0.955	1.1220	0.501	0.055	-1.373	0.073	-1.538	-0.050	-1.601	(14)

⁽¹⁾ $\log \text{mol L}^{-1}$; (2) $\log \text{Papp } (10^{-6} \text{ cm s}^{-1})$; (3) %; (4) $\log \text{Kp}$; (5) Yes/No; (6) $\log \text{L kg}^{-1}$; (7) $\log \text{BB}$; (8) $\log \text{PS}$; (9) $\log \text{mL min}^{-1} \text{ kg}^{-1}$; (10) $\log \text{mg kg}^{-1} \text{ day}^{-1}$; (11) $\log \text{kg}^{-1}$; (12) $\log \text{mg kg}^{-1} \text{ bw}^{-1} \text{ day}^{-1}$; (13) $\log \text{pg L}^{-1}$; (14) $\log \text{mM}$.

3.4 QSARIS-based physicochemical properties

Table 6 summarizes the physicochemical properties of the compounds retrieved from the QSARIS system and the number of hydrogen bonds (counted from docking-based results). In reference to Lipinski's rule of five, all the compounds are considered with drug-likeness regarding the criteria molecular mass (<500 amu) and total hydrogen-like counts (<5; either donating or accepting). However, that partition coefficient needs more deliberation as all the compounds register relatively high values compared to the threshold recommended ($\log P < +$ 5). This is understandable

since these are essence-based components, thus dispersed better in non-aqueous partition (i.e. octane) than the aqueous counterpart. Among the potential inhibitors, **23** (log P 1.31) is the most suitable one for biocompatible application; also, **24–26** (log P ca. 4) are acceptable. In contrast, **19**, **22**, and **27** (log P > 6) are clearly not preferred from this argument. In terms of polarizability, **26** registers a value of significance of 45.7 ų (only after that of **27**); that of **23** is also considered significant, 32.8 ų. In principle, the value measures the sensitivity of a chemical structure to external electric fields; particularly in the scope of this work, those created by protein structures (which are built up by polarized amino acids) or by electric double layers. By convention, the

Table 9: ADMET-based pharmacokinetics and pharmacology of 19-27 and D1-D2

Property	19	20	21	22	23	24	25	26	27	D1	D2	Unit
Absorption												
Water solubility	-7.835	-7.522	-7.525	-7.594	-3.975	-6.024	-5.844	-4.734	-8.517	-2.471	-2.162	(1)
Caco2 permeability	1.501	1.614	1.608	1.601	1.320	1.627	1.641	1.032	1.216	0.934	0.531	(2)
Intestinal absorption	91.195	91.793	92.241	91.735	95.033	98.235	98.38	97.702	90.341	74.469	53.464	(3)
Skin Permeability	-2.691	-2.768	-2.774	-2.805	-3.768	-2.734	-2.762	-4.057	-2.768	-3.177	-2.735	(4)
P-glycoprotein substrate	No	Yes	No	No	No	(5)						
P-glycoprotein I inhibitor	No	No	No	No	No	No	Yes	Yes	No	No	No	(5)
P-glycoprotein II inhibitor	No	Yes	Yes	Yes	No	No	No	Yes	Yes	No	No	(5)
Distribution												
VDss	0.399	0.272	0.306	0.332	0.297	0.199	0.314	-0.170	0.411	0.043	0.581	(6)
Fraction unbound	0.01	0.011	0.015	0.015	0.274	0.005	0.009	0.076	0.002	0.592	0.670	(6)
BBB permeability	0.81	0.786	0.776	0.786	-0.062	0.058	0.659	-0.796	0.981	-0.693	-1.057	(7)
CNS permeability	-1.394	-1.339	-1.562	-1.615	-1.984	-1.685	-1.752	-2.257	-0.955	-3.111	-3.761	(8)
Metabolism												
CYP2D6 substrate	No	(5)										
CYP3A4 substrate	Yes	No	No	(5)								
CYP1A2 inhibitor	Yes	Yes	Yes	Yes	No	Yes	Yes	No	No	No	No	(5)
CYP2C19 inhibitor	No	(5)										
CYP2C9 inhibitor	No	(5)										
CYP2D6 inhibitor	No	(5)										
CYP3A4 inhibitor	No	(5)										
Excretion												
Total Clearance	0.237	1.775	2.080	2.030	0.948	1.209	1.073	0.748	1.791	0.923	0.203	(9)
Renal OCT2 substrate	No	No	No	No	Yes	No	No	No	No	No	No	(5)
Toxicity												
AMES toxicity	No	(5)										
Max. tolerated dose	-0.172	0.058	0.009	0.070	-0.304	-0.869	-0.808	-0.596	-0.393	0.479	0.280	(10)
hERG I inhibitor	No	(5)										
hERG II inhibitor	Yes	No	Yes	No	No	(5)						
Oral rat acute toxicity	1.769	1.639	1.644	1.663	1.701	1.677	1.953	2.045	1.848	2.677	2.158	(11)
Oral rat chronic toxicity	1.048	3.13	3.025	3.097	1.649	2.317	2.077	0.141	0.946	1.091	2.832	(12)
Hepatotoxicity	No	No	No	No	No	Yes	Yes	No	No	No	Yes	(5)
Skin sensitization	Yes	Yes	Yes	Yes	No	Yes	Yes	No	No	No	No	(5)
T. pyriformis toxicity	0.637	1.445	1.497	1.417	0.781	0.853	1.31	0.401	0.464	0.106	0.285	(13)
Minnow toxicity	-1.717	-1.896	-1.765	-1.892	1.724	-0.561	-0.583	0.343	-3.485	2.31	3.386	(14)

(1) log mol L⁻¹; (2) log Papp (10^{-6} cm s⁻¹); (3) %; (4) log Kp; (5) Yes/No; (6) log L kg⁻¹; (7) log BB; (8) log PS; (9) log mL min⁻¹ kg⁻¹; (10) log mg kg⁻¹ day⁻¹; (11) log mg kg⁻¹ day⁻¹; (13) log μ g L⁻¹; (14) log mM.

unit dimension is converted following the Clausius–Mossotti relation: $10^6/4\pi\varepsilon_0~[A^2~s^4~kg^{-1}]$ =1[cm³]) [48].

3.5 ADMET-based pharmacokinetics and pharmacology

The pharmacokinetic characteristics of the candidates are presented in Table 7 (1–9), Table 8 (10–18), and Table 9 (19–27 and D1–D2); in each table, the properties are categorized into ADMET. Regarding toxicity: (i) almost no mutagenic potentials (except for 17); (ii) almost no potential for fatal ventricular arrhythmia as hERG inhibitors

(except for **19** and **27**); (ii) almost no potential for hepatotoxicity (except for **15**, **17**, **24**, and **25**); (iv) almost having skin sensitization (as oil-based characteristics); (v) certain toxicity to bacterium *T. pyriformis* (pIGC50 > $-0.5\log \mu g L^{-1}$) and fish Flathead Minnows (LC50 > -0.3). Nevertheless, the most promising bio-inhibitors, aka. **23** and **26**, are expected to express none of these negative effects against the body. Besides, the former is predicted to be under the disposition (renal clearance) by Organic Cation Transporter 2; none of the two is predicted to inhibit the activity of the cytochromes P450 family, yet to be oxidized by the liver (as CYP3A4 substrate). Regarding the distribution, **23** and **26** are plasma-tissue balanced, moderately cross the bloodbrain barrier, and partially penetrate the central nervous

system. Regarding absorption, **23** has no significant interaction with P-glycoprotein, thus no effects on the extrusion of the toxins and xenobiotics out of cells, while **26** is predicted otherwise. Both can be absorbed easily via intestinal routine (>95%). In general, *C. sahuynhensis* essence is a safe source of natural products for humans; in particular, **23** and **26** express high suitability for further drug-like development.

4 Conclusion

This is the first computer-based effort to screen for the antiviral potentiality of *C. sahuynhensis n-*hexane fraction (1-27), particularly against H5 HA in influenza A virus (PDB-5E32), wild-variant SARS-CoV-2 main protease (PDB-6LU7), and SARS-CoV-2 Omicron spike protein (PDB-7T9]). A combination of computational platforms specifies the most promising bio-inhibitors based on theoretical arguments from quantum calculations, docking simulations, and QSARbased analyses, i.e., 23 (bio-compatibility: ground energy -966.73 a.u., dipole moment 3.708 Debye; bio-inhibitability: \overline{DS} -12.5 kcal mol⁻¹; drug-likeness: mass 304.7 amu, log P 1.31; polar-interactability: polarizability 32.8 Å³) and **26** (bio-compatibility: ground energy -1393.66109 a.u., dipole moment 5.087 Debye; bio-inhibitability: DS −11.9 kcal mol⁻¹; drug-likeness: mass 437.5 amu, log P 4.28; polar-interactability: polarizability 45.7 Å³). The compounds also have favorable pharmacokinetics and pharmacology (based on the pkCSM-ADMET model). The total essence is ineffective for use as an antiviral source in its pure form since the most promising candidates account for minor proportions. Altogether, the results from this theoretical study encourage further isolation and preclinical tests for antiviral activities on 23 (7β-hydroxydehydroepiandrosterone) and 26 (ethyl cholate).

Acknowledgments: The authors thank the partial support of the Faculty of Traditional Medicine, University of Medicine and Pharmacy at Ho Chi Minh City, Vietnam, for the sample preparation and extraction.

Funding information: This work was supported by the Vietnam National Foundation for Science and Technology Development (NAFOSTED) (grant number 02/2020/ĐX); Hue University (grant number DHH2022-01-198).

Author contributions: N.T.T. – conceptualization; D.T.Q., D-C.T. – data curation; P.T.Q., T.Q.B., N.T.A.N. – formal analysis; P.T.Q., T.Q.B., L.N.H.D. – investigation; N.M.T., T.V.C. – methodology; N.M.T. – software; N.T.A.N. – supervision;

N.V.P. – visualization; P.T.Q., T.Q.B. – writing – original draft; D.T.Q., N.T.A.N. – writing – review and editing.

Conflict of interest: On behalf of all authors, the corresponding author states that there is no conflict of interest.

Ethical approval: The conducted research is not related to either human or animal use.

Data availability statement: All data generated or analyzed during this study are included in this published article (and its supplementary information file).

References

- [1] Binh QN, Tuan AH, Dat VN, Thanh TVT, Hanh PN, Cuong MN, et al. A new record Species for Flora of Vietnam-Curcuma singularis Gagnep. (Zingiberaceae). VNU | Sci Nat Sci Technol. 2017;33:25-9.
- [2] Kress WJ, Prince LM, Williams KJ. The phylogeny and a new classification of the gingers (Zingiberaceae): evidence from molecular data. Am J Bot. 2002;89:1682–96. Wiley Online Library.
- [3] Leong-Škorničková J, Newman M. Gingers of Cambodia, Laos & Vietnam. Singapore Botanic Gardens, National Parks Board Singapore; 2015.
- [4] Dosoky NS, Setzer WN. Chemical composition and biological activities of essential oils of Curcuma species. Nutrients. 2018;10:1196. MDPI.
- [5] Leong-Škorničková J, Lý N-S, Nguyễn QB. Curcuma arida and C. sahuynhensis, two new species from subgenus Ecomata (Zingiberaceae) from Vietnam. Phytotaxa. 2015;192:181–9.
- [6] Sam LN, Huong LT, Minh PN, Vinh BT, Dai DN, Setzer WN, et al. Chemical composition and antimicrobial activity of the rhizome essential oil of Curcuma sahuynhensis from Vietnam. J Essent Oil Bear Plants. 2020;23:803–9. Taylor & Francis.
- [7] Van Chen T, Lam DNX, Thong CLT, Nguyen DD, Nhi NTT, Triet NT. Morphological characters, pharmacognostical parameters, and preliminary phytochemical screening of Curcuma sahuynhensis Škorni? k. & NS Lý in Quang Ngai Province, Vietnam. Biodiversitas J Biol Divers. 2022;23:3907–20.
- [8] Marchese A, Arciola CR, Barbieri R, Silva AS, Nabavi SF, Tsetegho Sokeng AJ, et al. Update on monoterpenes as antimicrobial agents: A particular focus on p-cymene. Mater (Basel). 2017;10:947. MDPI.
- [9] Lau SKP, Poon RWS, Wong BHL, Wang M, Huang Y, Xu H, et al. Coexistence of different genotypes in the same bat and serological characterization of Rousettus bat coronavirus HKU9 belonging to a novel Betacoronavirus subgroup. J Virol Am Soc Microbiol. 2010;84:11385–94.
- [10] Sobrinho ACN, de Morais SM, Marinho MM, de Souza NV, Lima DM. Antiviral activity on the Zika virus and larvicidal activity on the Aedes spp. of Lippia alba essential oil and β-caryophyllene. Ind Crop Prod. 2021;162:113281. Elsevier.
- [11] Olivon F, Palenzuela H, Girard-Valenciennes E, Neyts J, Pannecouque C, Roussi F, et al. Antiviral activity of flexibilane and tigliane diterpenoids from Stillingia lineata. J Nat Prod. 2015;78:1119–28. ACS Publications.

- [12] Ge M, Wang H, Zhang G, Yu S, Li Y. The antiviral effect of jiadifenoic acids C against coxsackievirus B3. Acta Pharm Sin B. 2014;4:277-83. Flsevier
- [13] Yeh T-T, Wang S-K, Dai C-F, Duh C-Y. Briacavatolides A-C, new briaranes from the Taiwanese octocoral Briareum excavatum. Mar Drugs. 2012;10:1019-26. MDPI.
- [14] Zhang Y, Xu C, Zhang H, Liu GD, Xue C, Cao Y. Targeting hemagglutinin: approaches for broad protection against the influenza A virus. Viruses. 2019;11:405. MDPI.
- [15] Lin YP, Gregory V, Collins P, Kloess J, Wharton S, Cattle N, et al. Neuraminidase receptor binding variants of human influenza A (H3N2) viruses resulting from substitution of aspartic acid 151 in the catalytic site: a role in virus attachment? J Virol Am Soc Microbiol. 2010:84:6769-81.
- [16] Jin Z, Du X, Xu Y, Deng Y, Liu M, Zhao Y, et al. Structure of Mpro from SARS-CoV-2 and discovery of its inhibitors. Nature. 2020;582:289-93. London, UK: Nature Publishing Group.
- [17] Verma S, Patel CN, Chandra M. Identification of novel inhibitors of SARS-CoV-2 main protease (Mpro) from Withania sp. by molecular docking and molecular dynamics simulation. J Comput Chem. 2021;42:1861-72. Wiley Online Library.
- [18] Zhang L, Lin D, Sun X, Curth U, Drosten C, Sauerhering L, et al. Crystal structure of SARS-CoV-2 main protease provides a basis for design of improved a-ketoamide inhibitors. Science (80-). 2020;368:409-12. American Association for the Advancement of
- [19] Cui J, Li F, Shi Z-L. Origin and evolution of pathogenic coronaviruses. Nat Rev Microbiol. 2019;17:181-92. Nature Publishing Group.
- [20] Walls AC, Park Y-J, Tortorici MA, Wall A, McGuire AT, Veesler D. Structure, function, and antigenicity of the SARS-CoV-2 spike glycoprotein. Cell. 2020;181:281-92. Elsevier.
- [21] Ahmed SA, Abdelrheem DA, El-Mageed HRA, Mohamed HS, Rahman AA, Elsayed KNM, et al. Destabilizing the structural integrity of COVID-19 by caulerpin and its derivatives along with some antiviral drugs: An in silico approaches for a combination therapy. Struct Chem. 2020;31:2391–412.
- [22] Abdelrheem DA, Rahman AA, Elsayed KNM, Abd El-Mageed HR, Mohamed HS. Ahmed SA. Isolation, characterization, in vitro anticancer activity, dft calculations, molecular docking, bioactivity score, drug-likeness and admet studies of eight phytoconstituents from brown alga sargassum platycarpum. J Mol Struct. 2021;1225:129245. Elsevier.
- [23] Ahmed Atto Al-Shuaeeb R, Abd El-Mageed HR, Ahmed S, Mohamed HS, Hamza ZS, Rafi MO, et al. In silico investigation and potential therapeutic approaches of isoquinoline alkaloids for neurodegenerative diseases: computer-aided drug design perspective. J Biomol Struct Dyn. 2023;1-13. Taylor & Francis.
- [24] Al-Shuaeeb RAA, Abd El-Mageed HR, Ahmed SA, Mohamed HS, Hamza ZS, Rafi MO, et al. Identification of potent COVID-19 main protease inhibitors by loading of favipiravir on Mg12O12 and Zn12O12 nanoclusters: an in silico strategy for COVID-19 treatment. J Biomol Struct Dyn. 2022;1-13. Taylor & Francis.
- [25] Fan J, Fu A, Zhang L. Progress in molecular docking. Quant Biol. 2019;7:83-9. Springer.
- [26] Kapetanovic IM. Computer-aided drug discovery and development (CADDD): In silico-chemico-biological approach. Chem Biol Interact. 2008;171:165-76.

- [27] Frisch MJ, Trucks GW, Schlegel HB, Scuseria GE, Robb MA, Cheeseman JR, et al. Gaussian 09, Revision A.02. 2009.
- [28] Kassel LS. Density-functional exchange-energy approximation with correct asymptotic behavior. Phys Rev A. 1988;38:3098-100.
- [29] Schäfer A, Horn H, Ahlrichs R. Fully optimized contracted Gaussian basis sets for atoms Li to Kr. J Chem Phys. 1992;97:2571-7.
- [30] Molecular Operating Environment (MOE), 2015.02 Chemical Computing Group ULC, 1010 Sherbooke St. West, Suite #910, Montreal, QC, Canada, H3A 2R7; 2015.
- [31] Gasteiger J, Marsili M. Iterative partial equalization of orbital electronegativity-a rapid access to atomic charges. Tetrahedron. 1980;36:3219-28.
- [32] Lipinski CA, Lombardo F, Dominy BW, Feeney PJ. Experimental and computational approaches to estimate solubility and permeability in drug discovery and development settings. Adv Drug Deliv Rev. 1997;23:3-25.
- [33] Ahsan MJ, Samy JG, Khalilullah H, Nomani MS, Saraswat P, Gaur R, et al. Molecular properties prediction and synthesis of novel 1,3,4oxadiazole analogues as potent antimicrobial and antitubercular agents. Bioorg Med Chem Lett., 2011;21:7246-50. Elsevier Ltd.
- [34] Mazumdera J, Chakraborty R, Sena S, Vadrab S, Dec B, Ravi TK. Synthesis and biological evaluation of some novel quinoxalinyl triazole derivatives. Der Pharma Chem. 2009;1:188-98.
- [35] Pires DEV, Blundell TL, Ascher DB. pkCSM: Predicting small-molecule pharmacokinetic and toxicity properties using graph-based signatures. J Med Chem. 2015;58:4066-72.
- [36] Saeed NM, El-Demerdash E, Abdel-Rahman HM, Algandaby MM, Al-Abbasi FA, Abdel-Naim AB. Anti-inflammatory activity of methyl palmitate and ethyl palmitate in different experimental rat models. Toxicol Appl Pharmacol. 2012;264:84-93. Elsevier.
- [37] Jaleel GAA, Azab SS, El-Bakly WM, Hassan A. Methyl palmitate attenuates adjuvant induced arthritis in rats by decrease of CD68 synovial macrophages. Biomed Pharmacother. 2021;137:111347.
- [38] Wang YN, Wang HX, Shen ZJ, Zhao LL, Clarke SR, Sun JH, et al. Methyl palmitate, an acaricidal compound occurring in green walnut husks. J Econ Entomol. 2009;102:196-202. Oxford, UK: Oxford University Press.
- [39] Arora S, Kumar G. Phytochemical screening of root, stem and leaves of Cenchrus biflorus Roxb. I Pharmacogn Phytochem. 2018:7:1445-50. AkiNik Publications.
- [40] Arab HH, Salama SA, Eid AH, Kabel AM, Shahin NN. Targeting MAPKs, NF-kB, and PI3K/AKT pathways by methyl palmitate ameliorates ethanol-induced gastric mucosal injury in rats. J Cell Physiol. 2019;234:22424-38. Wiley Online Library.
- [41] Gohar YM, El-Naggar MMA, Soliman MK, Barakat KM. Characterization of marine Burkholderia cepacia antibacterial agents. J Nat Prod. 2010;3:86-94.
- [42] Hong SS, Choi CW, Lee JE, Jung YW, Lee JA, Jeong W, et al. Bioassayguided isolation and identification of anti-obesity phytochemicals from fruits of Amomum tsao-ko. Appl Biol Chem. 2021;64:1-8. SpringerOpen.
- [43] Ko G-A, Shrestha S, Kim Cho S. Sageretia thea fruit extracts rich in methyl linoleate and methyl linolenate downregulate melanogenesis via the Akt/GSK3β signaling pathway. Nutr Res Pract. 2018;12:3-12. The Korean Nutrition Society and the Korean Society of Community Nutrition.
- [44] Koo HJ, Park HJ, Byeon HE, Kwak JH, Um SH, Kwon ST, et al. Chinese Yam extracts containing B-sitosterol and ethyl linoleate protect against atherosclerosis in apolipoprotein E-deficient mice and

- inhibit muscular expression of VCAM-1 in vitro. J Food Sci. 2014;79:H719-29. Wiley Online Library.
- [45] Park SY, Seetharaman R, Ko MJ, Kim TH, Yoon MK, Kwak JH, et al. Ethyl linoleate from garlic attenuates lipopolysaccharide-induced pro-inflammatory cytokine production by inducing heme oxygenase-1 in RAW264. 7 cells. Int Immunopharmacol. 2014;19:253-61.
- [46] Chan P-M, Kanagasabapathy G, Tan Y-S, Sabaratnam V, Kuppusamy UR. Amauroderma rugosum (Blume & T. Nees) Torrend: Nutritional composition and antioxidant and potential
- anti-inflammatory properties. Evid-Based Complement Altern Med. 2013;2013:304713. Hindawi.
- [47] Rad AS, Ardjmand M, Esfahani MR, Khodashenas B. DFT calculations towards the geometry optimization, electronic structure, infrared spectroscopy and UV-vis analyses of Favipiravir adsorption on the first-row transition metals doped fullerenes; a new strategy for COVID-19 therapy. Spectrochim Acta Part A Mol Biomol Spectrosc. 2021;247:Article ID 119082. Elsevier.
- [48] Feynman R. The Feynman lectures on physics Volume II. Millenium. In: Gottlieb MA, editor. New York: Basic Books; 2010.